

Chapter 7

Influence of the geomagnetic field on extensive air shower muons

7.1 Introduction

This is a well known fact that EAS parameters like N_e , N_μ , X_{\max} and the s have shown their sensitivity to the CR mass composition. Measurement of all these parameters are made either by individual or hybrid detection technique. The observation of an EAS provides electron and muon LDD at the observational level. As we have discussed in our previous chapters that the observed LDD data are reconstructed by means of lateral density function such as NKG structure function [1] in order to get different EAS observables. The radial distribution of cascade particles in an average EAS is generally assumed to be symmetrical in the plane perpendicular to the shower axis. But, presence of intrinsic fluctuations (due to stochastic nature of EAS development) from shower to shower, in addition, higher zenith angles (here, $\Theta \geq 50^\circ$) and geomagnetic effects can perturb this axial symmetry noticeably. Such effects may even distort the axial symmetry a little to the distribution of EAS particles even in vertically incident showers. Inclined showers though experience similar effects as vertical showers but manifest significantly large asymmetries.

Disregarding the geomagnetic effect, in ground array experiments the analysis of the density data is usually performed by assuming axial symmetry. Therefore, asymmetries would come from the polar variation of EAS charged particles and unequal attenuation accounted from different hits of the EAS on the ground

plane with inclined incidence. These are known as geometrical and atmospheric attenuation effects to polar asymmetries. To accentuate the geomagnetic effects on the EAS charged particle distribution alone, the geometric and attenuation effects must be isolated or corrected out in the analysis. The data analysis technique which we are going to introduce here will remove the polar asymmetry caused by the geometric effect, while the asymmetry resulting from the attenuation effect would be ignored judiciously as muons suffer very little attenuation in the atmosphere. In this work, it is shown that the asymmetry arises in polar distribution of muons predominantly from the geomagnetic field (GF), may explore a new possibility for the determination of the mass composition of CRs.

In this chapter, we address the influence of the GF on the spatial distribution of muons with a general limit on the zenith angle ($\geq 50^\circ$), valid for all applications of the technique, choosing the KASCADE experiment [2] site and look at the charge separation between the positive (μ^+) and negative (μ^-) muons to arrive at a possible mass dependent parameter, called the *transverse muon barycenter separation* (TMBS). This TMBS is expected to be dependent on the nature of the primary particle and hence, in principle, the parameter can be exploited to estimate primary mass. The method presented here is applied to Monte Carlo data simulated in three limited primary energy regions: 1 – 3, 8 – 12 and 98 – 102 PeV (to obtain sufficient number of EAS events at these narrow energy regions by the available computing power). The analysis described in this work is based on Monte Carlo simulations carried out with the code *CORSIKA* [3]. We also discuss the practical realization of the proposed method in a real experiment.

In this chapter, the basics of the influence of the GF on the EAS cascade, which are of direct relevance to this work, is discussed in the following section 7.2. In section 7.3, we report on the simulation procedure adapted here. The MC data analysis technique is discussed in section 7.4. In section 7.5, we present our results with discussion obtained from geomagnetic effects on EAS muons. After quantifying the asymmetry of EAS muons in presence of the GF we have made an effort to correlate the asymmetry parameter with GFs at different geographical locations in the world, which is included in 7.5. A possible experimental approach of the present method and concluding remarks are pointed out in section 7.6.

7.2 Influence of the geomagnetic field on EAS cascade

It is well known that the GF causes the East-West asymmetry on the primary CRs according to their rigidity and energy. The study of CRs with primary energies above 0.1 PeV is usually based on the measurements of EASs, which are essentially cascades of secondary particles produced by interactions of CR particles with atmospheric nuclei. During the development of a CR cascade in the atmosphere, the GF affects the propagation of secondary charged particles in the shower: the perpendicular component of this field causes the trajectories of secondary charged particles to become curved, with positive and negative charged particles deflecting to produce a overall transverse barycenter separation. This aspect was first pointed out by Cocconi nearly sixty two years back [4]. He further suggested that the geomagnetic broadening effect can be non-negligible in compare to the Coulomb scattering, particularly for the young showers. Since then, several studies have been carried out to address the influence of the GF on CR EAS and some important effects arising out of it were also reported (see for instance [5–21] and references therein). We should however state that some of these effects of the GF mentioned in those references have no direct relevance to this particular study.

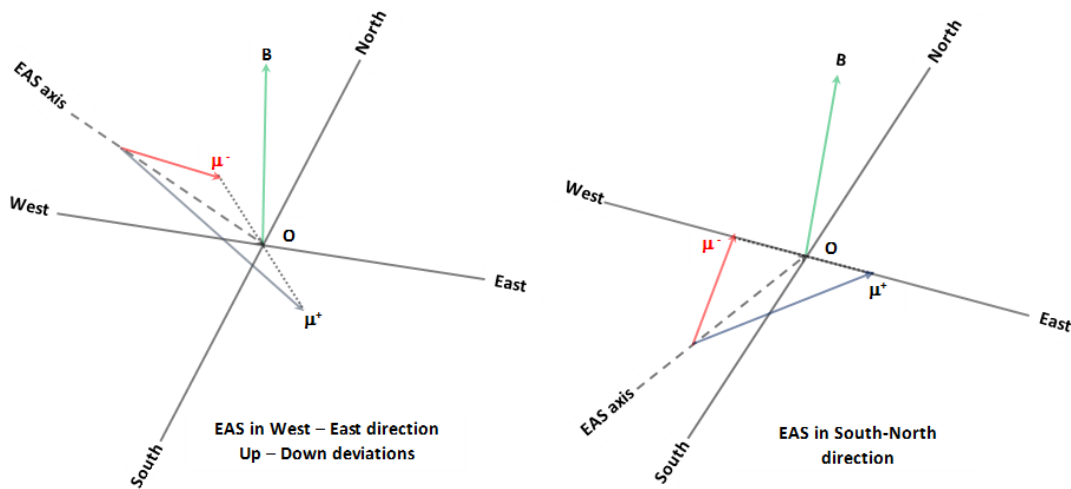


FIGURE 7.1: The separation of μ^+ and μ^- generated from a parent particle in an EAS by the geomagnetic field in two different situations.

For the soft component i.e. electrons, the radiation lengths in the atmosphere are short and they suffer many scatterings with $E_{e^\pm} < E_{cr.}$ (where $E_{cr.}$ be the critical energy of electrons, which is ≈ 84 MeV in air) and stronger *bremsstrahlung*

effect (when $E_{e\pm} > E_{cr.}$) thereby randomly changing the directions of their momenta relative to the GF. These processes are responsible for the lateral spread of electrons in the EAS, while the effect of GF on them is less pronounced [22]. In contrast, after their generation from pion and kaon decays (mainly those in first few generations from their parent particles at great atmospheric heights), muons travel much longer paths encountering negligible scattering with the medium (suffer lesser bremsstrahlung also), and hence come under the influence of GF noticeably. As a result, geomagnetic effect should be more pronounced on medium to high momenta muons than lower ones, particularly for very large and strongly inclined showers. Such a situation is depicted by the Fig. 7.1. The **left** figure is showing a separation between μ^+ and μ^- generated from a parent particle in an EAS coming from the West and advances into the East direction. But, the **right** figure shows a situation where the EAS comes from the South and advances into the North direction in the *CORSIKA* coordinate system. Besides, in highly inclined showers, a high percentage of EAS electrons is absorbed in the atmosphere, may reduce shower-to-shower fluctuations to a great extent. Exploiting this feature, some earlier Monte Carlo simulation studies [10] reported that heavy nuclei and proton induced showers may be discriminated from the elliptic footprint of lateral muon distribution and the muon charge ratio (the ratio of μ^+ to μ^- numbers) at convenient distances from the shower core. Through our preliminary study on this aspect of the GF, their prediction was substantiated and reported in International Conferences [23, 24] using simulations. This paper includes a comprehensive data analysis, and quantifies different new features from the analysis compared to earlier studies [10, 23, 24], in order to obtain the primary mass information by the geomagnetic effects.

7.3 Simulation of EAS

In the framework of the air shower simulation program *CORSIKA* of version 6.970 [3], the EAS events are simulated by combining the high energy (above 80GeV/n) hadronic interaction models QGSJet 01 version 1c [25] and EPOS 1.99 [26], and the low energy (below 80GeV/n) hadronic interaction model UrQMD [27]. The EGS4 program library is chosen for simulation of the EM-component of shower that incorporates all the major interactions of electrons and photons

[28]. We consider the US-standard atmospheric model with planar approximation, which works for Θ of the primary particles being less than 70° [29]. Events are generated at zenith angles $70^\circ < \Theta < 90^\circ$ with CURVED option of the atmosphere in the standard *CORSIKA* program [3]. The EAS events are simulated at the geographical location of the experimental site of KASCADE (latitude 49.1° N, longitude 8.4° E, 110 m a.s.l.) [2]. The GF with a homogeneous field approximation is considered. In order to examine the effect of the GF, EAS events are also simulated by switching off Earth's magnetic field. On the observation level, the detection kinetic energy thresholds are chosen as 3 MeV for electrons and 300 MeV for muons.

The EAS events are generated for proton (p) and iron (Fe) primaries at three different limited primary energy regions as mentioned in the section 7.1. At each energy range, we have taken five different narrow ranges of Θ , $48^\circ - 53^\circ$, $53^\circ - 58^\circ$, $58^\circ - 63^\circ$, $63^\circ - 68^\circ$ and $68^\circ - 69^\circ$ respectively with FLAT option. A small sample of EAS events are also simulated with a range $73^\circ - 78^\circ$ using the CURVED option of the atmosphere. In order to have at least some hints of fluctuations to our important observables, we have considered those limited ranges of energy (E) and Θ . If we simulate EAS events in a wider range instead (say, $0^\circ < \Theta < 70^\circ$), most of the events will then have Θ concentrating around $35^\circ - 45^\circ$ range, but for which muons will not remain a crucial component compare to other charged secondaries in the EAS. The proportion of muons in an EAS rises with increasing Θ relative to the EM component, and hence the GF on muons will be effective at higher Θ only. We have used thinning option of *CORSIKA* for the primary energy range 98 – 102 PeV by taking 10^{-6} as thinning factor according to the optimum weight limitation [30]. Showers are generated mostly over the whole azimuthal angle range ($\Phi = 0^\circ - 360^\circ$). We have also used a considerable number of showers generated at two fixed azimuthal angles: 0° and 90° for some results (only showers from the North and West directions in the coordinate system of *CORSIKA*). About 2×10^5 generated showers have been used in the present analyses.

7.4 Data analysis method and selection criteria

When the GF is disabled (setting B as $\sim 10^{-5}$ part smaller than the magnetic fields at the KASCADE location) in the simulation program, the lateral distribution of EAS charged particles possess cylindrical symmetry around the EAS axis in the shower front plane. In the observer plane, however, such cylindrical symmetry is distorted for inclined EAS due to the geometrical and the atmospheric attenuation effects. When the GF is switched on, the polar asymmetry arising from the geomagnetic effect is superimposed with those caused by the geometric and attenuation effects. Therefore, for isolating or correcting out the effect contributed by the GF from other two sources of distortion, the following part of this section has to be worked out during data analysis.

Observables such as the muon density (ρ_μ) or the truncated muon size ($N_\mu^{\text{tr.}}$) ($N_\mu^{\text{tr.}}$ accounts the total number of muons in a region with 60 – 90 m radial distance range from the EAS core and 10° or 15° polar angle bin) obtained from the analysis of simulated data get overestimated in the early region while underestimated in the late region of an EAS. Hence muons in the early region do undergo lesser attenuation than those arriving in the late region. This development feature of the EAS accounts the attenuation contribution to the overall polar asymmetry of the lateral distribution of muons, and is called the attenuation effect. The polar asymmetries are also present in EAS observables when the information of muons transforms from the observer plane to the more justified shower front plane. This asymmetry appears from another effect, and is known as the geometric effect. To extract these two asymmetries from the EAS observables, we have to implement the following corrections into the simulated data. The correction that results from the geometric effect can be briefly summarized by defining the relevant quantities involved. A projection procedure is applied for transforming the point of impact of each cascade particle from the observer plane onto the shower front plane. This will eventually transform the ρ_μ or $N_\mu^{\text{tr.}}$ from the ground plane onto the shower front plane. In the Fig. 7.2, we have shown the transformation of a point of impact by a muon in the the ground (* mark) having polar coordinates; (r_g, ϕ_g) onto the shower plane with the set of coordinates; $(r_s, \beta_s$ or $x_s, y_s)$. The necessary transformation relations are trivial and are as follows,

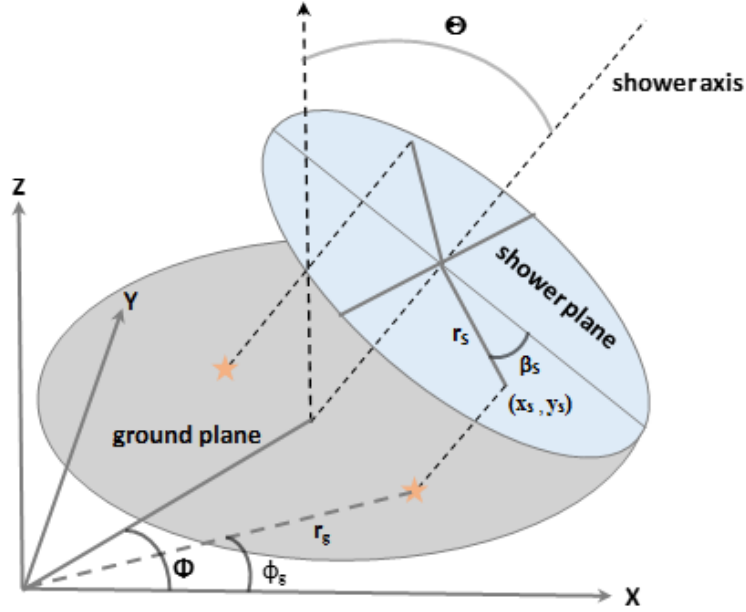


FIGURE 7.2: Sketch of the geometry of the ground plane and shower front plane used for the geometric correction in an inclined shower.

$$r_s = r_g \sqrt{1 - \sin^2 \Theta \cos^2(\phi_g - \Phi)}. \quad (7.1)$$

Using the Fig. 7.2, the corresponding Cartesian coordinates $P(x_s, y_s)$ at the shower front plane can be easily obtained as,

$$x_s = r_g \cos(\phi_g - \Phi) \cos \Theta \quad (7.2)$$

$$y_s = r_g \sin(\phi_g - \Phi) \quad (7.3)$$

In the geometric correction, interaction due to attenuation process suffered by muons is not considered in the region between the two planes. Then the muon density in the shower front plane ($\rho_s(r_s, \beta_s)$) can be obtained from the muon density measured in the observer plane ($\rho_g(r_g, \phi_g)$) by a simple geometrical transformation [31], and is given by

$$\rho_s^{\text{inaccur.}}(r_s, \beta_s) = \frac{\rho_g(r_g, \phi_g)}{\cos \Theta}. \quad (7.4)$$

This above equation for $\rho_s^{\text{inaccur.}}(r_s, \beta_s)$ is inaccurate because it does not reflect the effect of attenuation of muons in the space between the two planes.

An accurate measure for the muon density ($\rho_s^{\text{accur.}}(r_s, \beta_s)$) in the front plane taking the geometrical projection of $\rho_g(r_g, \phi_g)$ onto the shower front plane with attenuation correction is made possible by [31]

$$\rho_s^{\text{accur.}}(r_s, \beta_s) = \frac{\rho_g(r_g, \phi_g)}{\cos\Theta} \cdot e^{\pm(\eta x_g \sin\Theta)}, \quad (7.5)$$

where η is the attenuation length in the unit of the reciprocal of linear distance (η has values $\sim \frac{0.15}{190}$ and $\sim \frac{0.15}{900} \text{ m}^{-1}$ for electrons and muons respectively at the KASCADE level [32–34]). From the geometry of the cylindrical EAS profile, we have to substitute $\pm x_g \sin\Theta$ (-ve and +ve signs are taken corresponding to the attenuation of the late and early parts of the EAS respectively) for the additional path between the planes. The above equations 7.4 and 7.5 hold for the EASs coming from the North i.e. $\Phi = 0^\circ$. For an arbitrary Φ , one should replace ϕ_g by $\phi_g - \Phi$ only in relevant equations. We will now plot the ratio between the accurate and inaccurate muon densities versus the core distance (r_s) ($r_s = (x_g^2 \cos^2\Theta + y_g^2)^{\frac{1}{2}}$ [31]) using the simulated muon densities when $B \sim 10^{-5} \times B_{\text{KAS.}} \sim 0$. The same study is repeated for the simulated electron data as well. At $B \sim 0$, the ratio between the accurate and inaccurate muon or electron densities in the late part of the shower plane are shown in the Fig. 7.3 with r_s . The scattered points correspond the simulated density data while the lines are obtained using the equations 7.4 and 7.5 for cylinder model of EAS [31]. The figure clearly reflects the effect of attenuation on these two components in the concerned space. The figure indicates that the muon densities in the shower front plane with or without the attenuation corrections are nearly the same, and is negligibly smaller than what contributed by the charged EM component of an EAS. Hence, we may ignore the attenuation effect on the muon component from the space between two planes in our data analysis. We have also examined the average longitudinal development of electrons and muons for highly inclined showers to see the attenuation power between the EM and muonic components of EAS from the first interaction point to sea level atmospheric depth. The curves in the Fig. 7.4 illustrate how muon and electron contents of EAS vary during the evolution of an average EAS through the atmosphere. It is clear from the figure that the muon component remains nearly insulated from the atmospheric attenuation especially in the space between the two concerned planes. This particular study involves all the charged muons with $E_{\text{cut}}^\mu \geq 300 \text{ MeV}$, but rest of our results consider very energetic muons with $p_\mu \geq 100 \text{ GeV}/c$. Important reasons behind such momenta

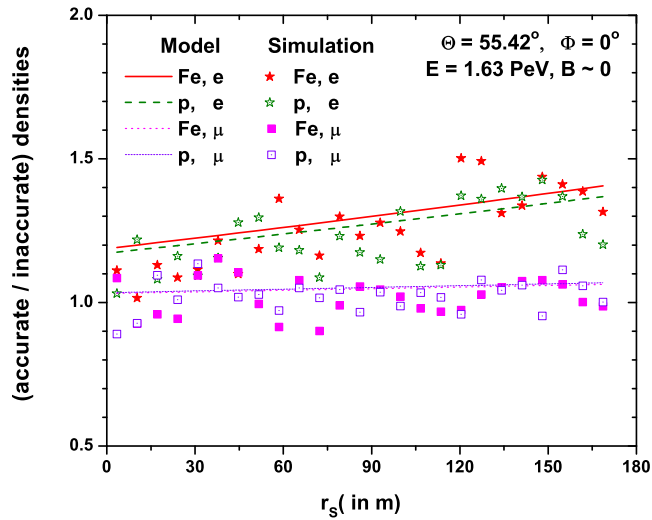


FIGURE 7.3: The ratios of the accurate (projection+attenuation - corrected) to the inaccurate (projection - corrected) densities for showers coming from the North with core distance in the shower front plane. Densities are taken from the core to the late part of showers.

selection will be discussed later. These energetic muons, generated from their parent particles at great atmospheric heights are expected to suffer very low attenuation. This result also reiterates the fact that the attenuation of the muon component is negligibly small. A very recent study on the atmospheric attenua-

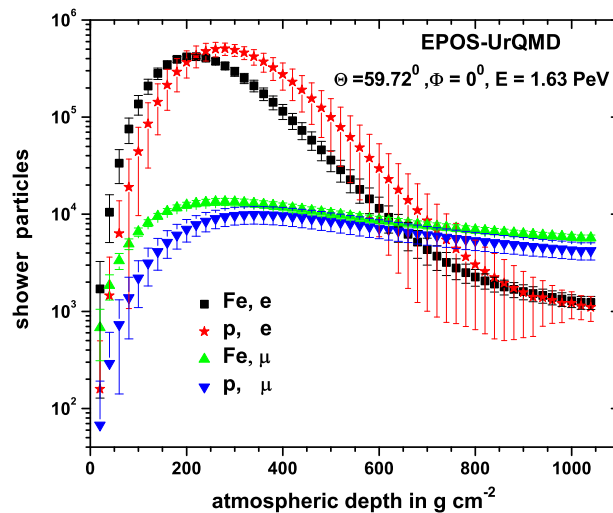


FIGURE 7.4: Average longitudinal distribution of electrons and muons for proton and iron induced showers.

tion of different charged components of EAS in the concerned space introducing a newly defined parameter, called ‘a shift’ of the EAS core, also agrees with

the insignificant trait of the attenuation effect from muons [31, 35]. All these above studies concerning the attenuation properties of muons indicate that this correction to simulated data could be ignored for our results. The present analysis selects muons which qualify two selection criteria simultaneously associated with muon detection area and muons energies or momenta. High-energy muons get going from the upper part of the atmosphere and hence experience the GF for a longer duration as they approaching the observer level. This is consistent with the expectations since the high momenta muons will survive against attenuation especially in highly inclined showers.

The main observables TMBS and MTMBS (maximum value of TMBS) are expected to be dependent upon the energy of incoming muons. This work has identified some suitable conditions for the detection and the measurement of these observables with reasonable muon numbers. This situation essentially demands a best compromise among the muon detector size, muon energy thresholds and the N_{μ}^{tr} . The noticeable effects of the GF are emphasized in the case of highly inclined showers with high momentum muons ($10^2 - 10^3$ GeV/c).

The practical realization of the present approach in the work requires a pair of muon detectors covering two finite regions in diagonally opposed positions, will be shown in the last Fig. 7.15 in conjunction with an EAS array containing several scintillation detectors. To use a statistically significant number of showers for our results, we have studied the frequency distribution of the azimuthal angle Φ from the generated showers corresponding to different smaller bins of Θ at a given small energy range. One such distribution is shown in the Fig. 7.5. The figure indicates that if we use showers coming around $\Phi_1 \sim 52.5^\circ$ and $\Phi_2 \sim 245^\circ$ directions then a certain level of statistical problem could be avoided. Hence, our analysis considers showers around these Φ_1 and Φ_2 with a small Φ -bin as $47.5^\circ - 57.5^\circ$ and $240^\circ - 250^\circ$. It is noteworthy to state that the azimuthal modulation of shower events around the two aforesaid azimuthal windows arises due to geomagnetic effect.

The work also foresees the employment of a pair of muon detectors into the array with some reasonable sizes from the point of view of their construction cost. We have used different combinations of momentum thresholds and muon detection areas as trials so that a better option may be surfaced, which will deliver an optimal asymmetry between μ^+ and μ^- particles. It has been seen that the

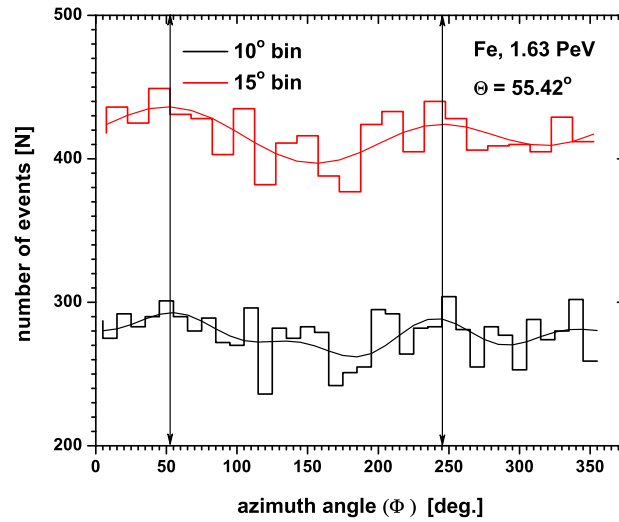


FIGURE 7.5: Distribution of the azimuth angle Φ for all simulated events (pre-selected). Events are selected from two smaller bins with size $\Delta\Phi \sim 10^\circ$ around two arrow heads vertical lines for further consideration in the analysis.

TABLE 7.1: Analysis showing an implementation of the selection of best possible muon detection regions in opposite sides keeping several factors in mind. Here, we have used Fe showers with $E = 98 - 102$ PeV, $\Theta = 63^\circ - 68^\circ$ and $\Phi = 47.5^\circ - 57.5^\circ$. The selection is made for charged muons with $p_\mu = 10^2 - 10^3$ GeV/c. Highlighted figures correspond qualified (Q) data from the selection - Y: Yes; N:No.

Muons	r -range (m)	$150^\circ - 195^\circ$ (%)	$330^\circ - 375^\circ$ (%)	Total - muons	Q
μ^+	30 – 60	34.75 ± 3.53	6.53 ± 8.91	2052	N
μ^-	30 – 60	6.55 ± 8.43	34.61 ± 3.60	2019	N
μ^+	60 – 90	38.27 ± 4.29	5.28 ± 9.47	1660	Y
μ^-	60 – 90	5.10 ± 10.34	38.45 ± 5.09	1646	Y
μ^+	90 – 120	41.47 ± 5.86	4.22 ± 14.29	1201	N
μ^-	90 – 120	4.12 ± 13.29	41.93 ± 5.76	1192	N

low momenta muons (below $\sim 10^2$ GeV/c) offer nearly symmetrical distribution in the X – Y shower plane, whereas muons with momenta falling in the range $10^2 - 10^3$ GeV/c manifest a better polar asymmetry in μ^+ and μ^- numbers in the annular region between 60 m and 90 m from the EAS core. Table 7.1 and Table 7.2 give a clear view on muons selection in accordance with the above requirement. The highlighted figures in both the tables correspond better combinations between muons thresholds and their detection areas, for which an optimum local contrast in the abundance of μ^+ and μ^- could be achieved. The relative errors associated with these percentages are provided in order to get an

TABLE 7.2: Analysis showing an implementation of the selection of muons momenta in selected detection regions obtained from Table 7.1. Here, we have used Fe showers with $E = 1 - 3, 8 - 12, \text{ and } 98 - 102 \text{ PeV}$, and $\Theta = 63^\circ - 68^\circ$, and $\Phi = 47.5^\circ - 57.5^\circ$. Highlighted figures correspond qualified data from the selection.

Muons	E (GeV)	p_μ (GeV/c)	$150^\circ - 195^\circ$ (%)	$330^\circ - 375^\circ$ (%)
μ^+	10^6	$1 - 10^2$	24.26 ± 39.21	10.21 ± 58.45
μ^-	10^6	$1 - 10^2$	11.42 ± 55.64	25.11 ± 38.90
μ^+	10^7	$1 - 10^2$	25.17 ± 10.10	11.41 ± 17.11
μ^-	10^7	$1 - 10^2$	10.55 ± 20.26	24.70 ± 11.88
μ^+	10^8	$1 - 10^2$	24.97 ± 6.39	10.48 ± 11.81
μ^-	10^8	$1 - 10^2$	11.29 ± 10.08	24.57 ± 6.78
μ^+	10^6	$10^2 - 10^3$	43.90 ± 26.22	4.32 ± 85.14
μ^-	10^6	$10^2 - 10^3$	4.06 ± 88.40	43.93 ± 26.83
μ^+	10^7	$10^2 - 10^3$	41.73 ± 8.21	4.46 ± 36.94
μ^-	10^7	$10^2 - 10^3$	4.70 ± 27.95	39.88 ± 12.32
μ^+	10^8	$10^2 - 10^3$	38.27 ± 4.29	5.28 ± 9.47
μ^-	10^8	$10^2 - 10^3$	5.10 ± 10.34	38.45 ± 5.09

indication of the significance of these percentage figures. Data other than highlighted ones in those tables would either provide lower percentage of μ^+ and μ^- abundances at two detector locations out of a relatively higher total or higher percentage of μ^+ and μ^- abundances at detector locations out of a relatively lower total. The error on these percentages also justify the above facts. Errors in the Table 7.2 in particular decrease with the increase of primary energy simply because of increasing muon number statistics. Other than highlighted combinations are found unsuitable for estimating TMBS and MTMBS with some anticipated uncertainties. In the upcoming sections, we shall consider only these selected muons having $p_\mu = 10^2 - 10^3 \text{ GeV/c}$ and $r = 60 - 90 \text{ m}$ in the further analysis for our important results.

7.5 Results and discussion

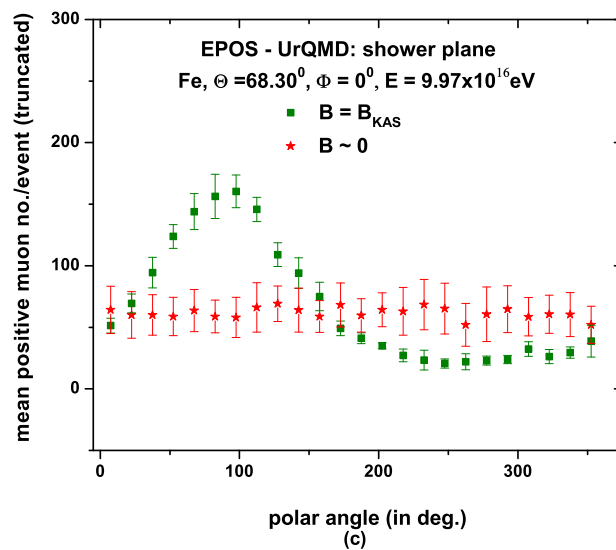
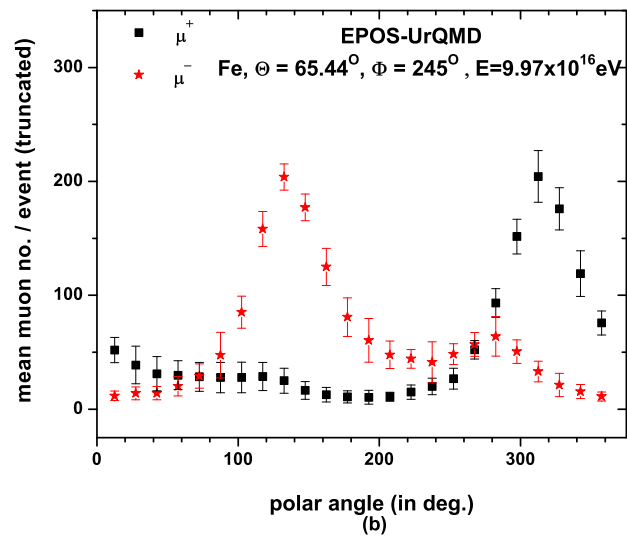
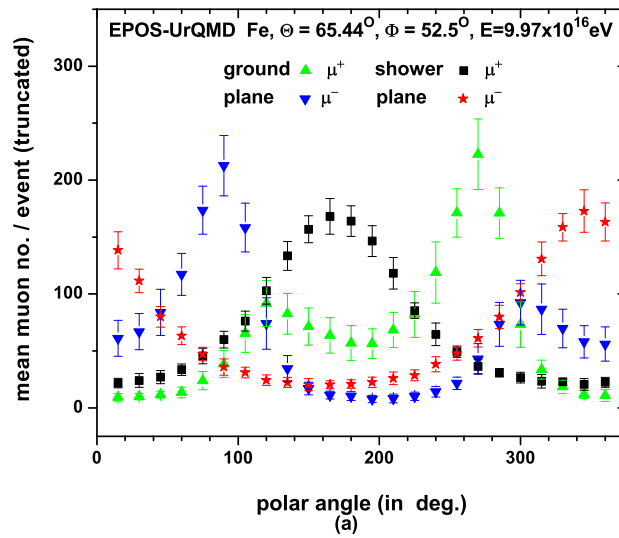
7.5.1 The polar asymmetries of the lateral distribution of EAS muons

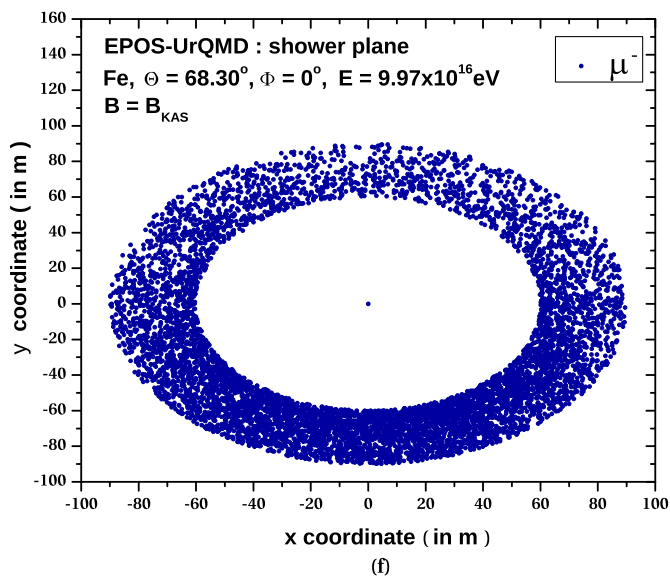
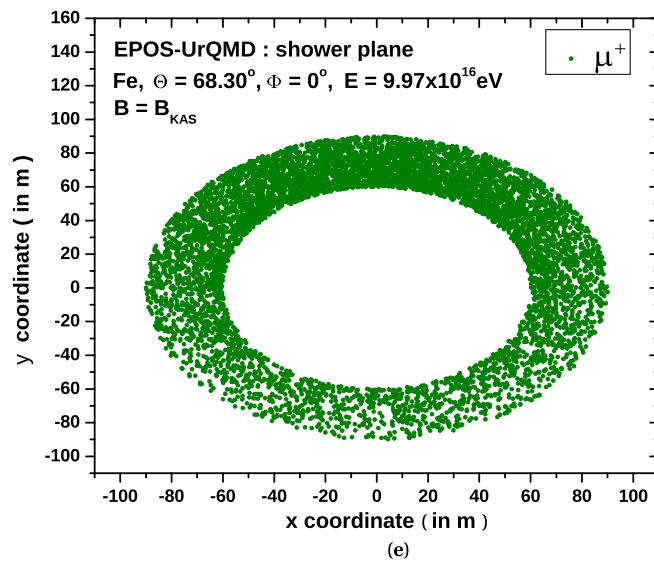
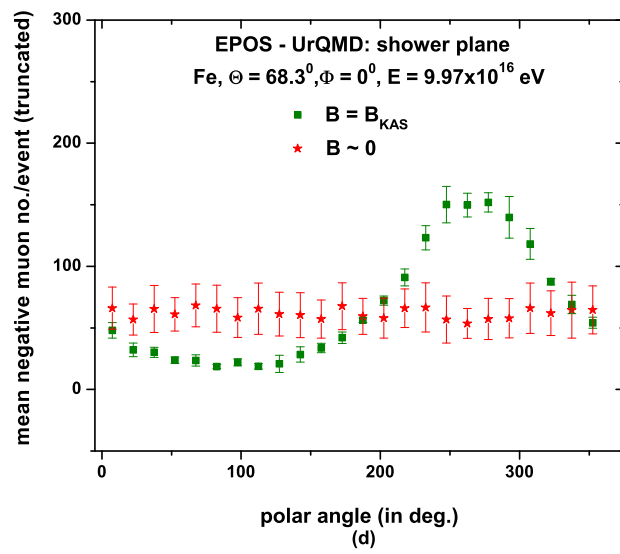
To examine the polar asymmetries of the lateral distributions of μ^+ and μ^- due to the GF, we have estimated total number of each variety of muons over an arc region of truncated core distance range of $60 - 90 \text{ m}$ and central angle 15° at different polar positions in both the planes (taking $p_\mu = 10^2 - 10^3 \text{ GeV/c}$). In the

Fig. 7.6a, the polar asymmetries of μ^+ and μ^- in both the planes are depicted for $\langle\Theta\rangle = 65.44^\circ$ and $\langle\Phi\rangle = 52.5^\circ$, while in the Fig. 7.6b, we have used different showers with $\langle\Phi\rangle = 245^\circ$, and the polar variation is limited to the shower plane only. For clear understanding of the influence of the GF, we have also studied the polar variations of μ^+ and μ^- independently for $B = B_{\text{KAS}}$ and $B \sim 0$. These are shown in Fig. 7.6c and Fig. 7.6d for Fe initiated showers corresponding to $\langle\Theta\rangle = 68.3^\circ$ and $\Phi = 0^\circ$. The nature of these polar variations are as per expectations. However, it should be mentioned that all these studies were also covered by other papers [12, 20], but authors used muon densities instead of number from different perspectives.

The Fig. 7.6a is a combined study on μ^+ and μ^- polar variations including the ground plane for B_{KAS} but at an arbitrary $\langle\Phi\rangle = 52.5^\circ$. Inclusion of the ground plane in the figure is merely for observing asymmetries compared to the shower plane. Our subsequent studies will not include the ground plane at all because it does not provide any additional information. The Fig. 7.6b represents the polar variations of μ^+ and μ^- for showers coming from the other arbitrary direction corresponding to $\langle\Phi\rangle = 245^\circ$. In the rest figures polar variations of μ^+ and μ^- are shown separately using accumulated and scattered plots respectively. It is noticed that the enhancements of μ^+ and μ^- occur around $\beta_s \sim 90^\circ$ and $\sim 270^\circ$ respectively when $\Phi = 0^\circ$. For $\langle\Phi\rangle = 52.5^\circ$ the enhancements are seen around $\beta_s \sim 165^\circ$ and $\sim 345^\circ$ while for $\langle\Phi\rangle = 245^\circ$, around $\beta_s \sim 132^\circ$ and $\sim 312^\circ$ indicate the prominent enhancement regions. These results particularly for $\langle\Phi\rangle = 52.5^\circ$ would therefore validate our selection of polar angle ranges which have been worked out in Table 7.1 and Table 7.2. Most of the figures cited above consider Fe initiated showers because of having dominant muon signals (a generic feature) over p and other nuclei initiated showers, which may receive noticeable influence from the GF.

In the following, a few relatively new EAS parameters concerning the polar asymmetry of charged muons due to GF will be defined, and their sensitivity to the primary mass will be analyzed. These mass sensitive parameters are namely the TMBS, MTMBS and the eccentricity (ϵ) of the elliptic lateral distribution of charged muons.





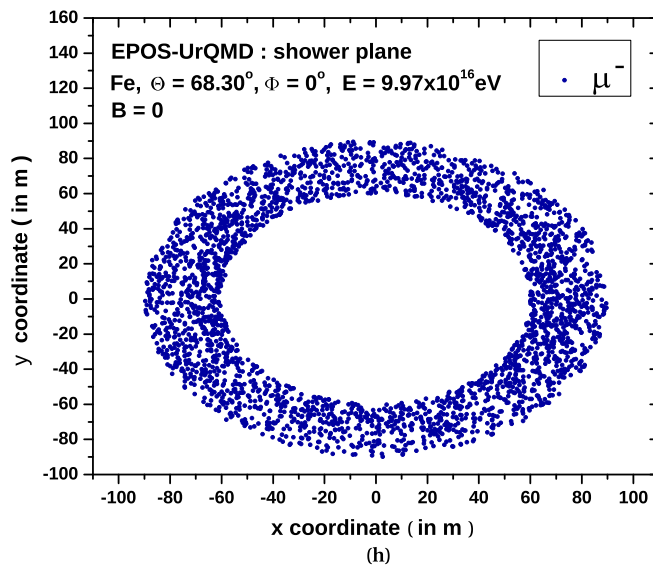
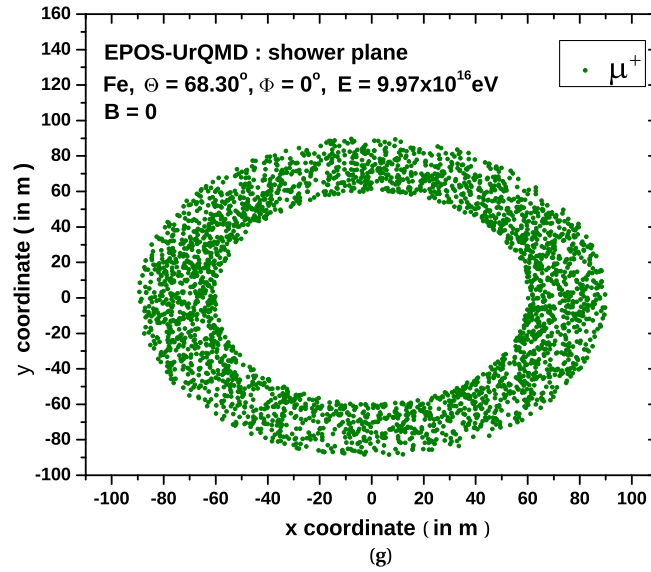


FIGURE 7.6: In Fig. 7.6a and Fig. 7.6b, we have used our two selected Φ ranges but keeping the mean Θ at 65.44° for the mean polar variations of μ^+ and μ^- for iron primary. The mean polar variations of μ^+ and μ^- and their corresponding scattered plots, are also shown independently in Fig. 7.6c, Fig. 7.6d, Fig. 7.6e, Fig. 7.6f, Fig. 7.6g and Fig. 7.6h when showers arriving from the very restrictive North direction. For Fig. 7.6a, the x-label represents both the polar angles; β_s and ϕ_g while for Figs. 7.6b, 7.6c, and 7.6d, X-axis represents β_s only.

7.5.2 The transverse muon barycenter separation and its maximum value

To quantify the influence of GF as well as to identify some typical signatures of the nature of shower initiating primaries, we have estimated for each shower the coordinates of barycenters of μ^+ and μ^- particles in the shower plane and thereby estimated the TMBS, which actually measures the separation length between the barycenter positions of μ^+ and μ^- . For this purpose, we have introduced an operation that involves a rotation either clockwise or anti-clockwise sense of a hypothetical interior quadrant sector (IQS) for counting the μ^+ and μ^- particles: the IQS is a region in the interior of a circle enclosed by a pair of arcs on opposite sides and a pair of diagonally aligned straight lines passing through the EAS core making a central angle of $\sim 15^\circ$. However, the implemented IQS in the work is taken from the truncated core distance range 60 – 90 m in two diagonally opposed regions (a sketch is provided in Fig. 7.7).

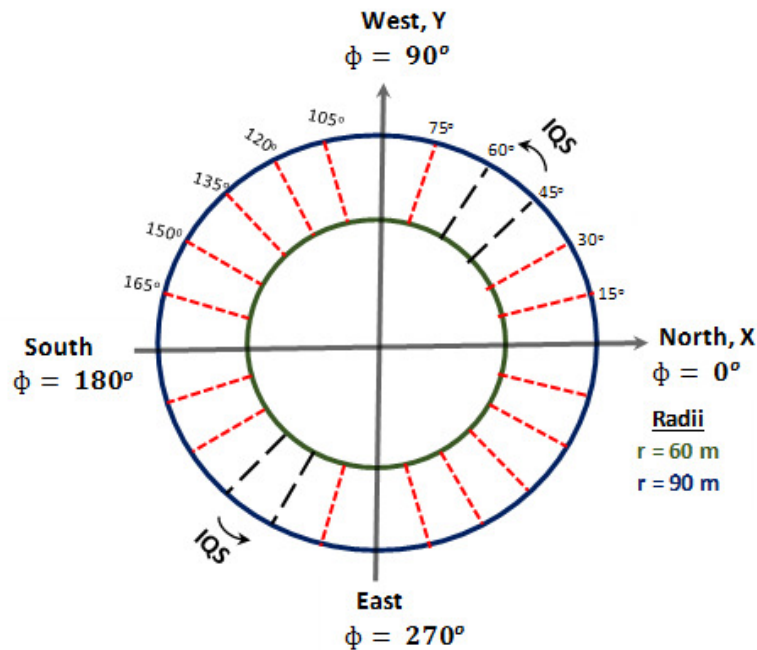


FIGURE 7.7: Scanning of μ^+ and μ^- particles by rotating IQS in anti-clockwise sense from 0° to 180° .

The variation of the TMBS with the rotation of IQS for p and Fe initiated EASs falling in the zenith angle range; $53^\circ - 78^\circ$ and arriving from two statistically significant directions, are studied using simulated data. In Fig. 7.8a and Fig. 7.8b, a comparison of these variations are shown for showers initiated by p and Fe primaries arriving within the azimuthal angle ranges; $47.5^\circ - 57.5^\circ$ and $240^\circ -$

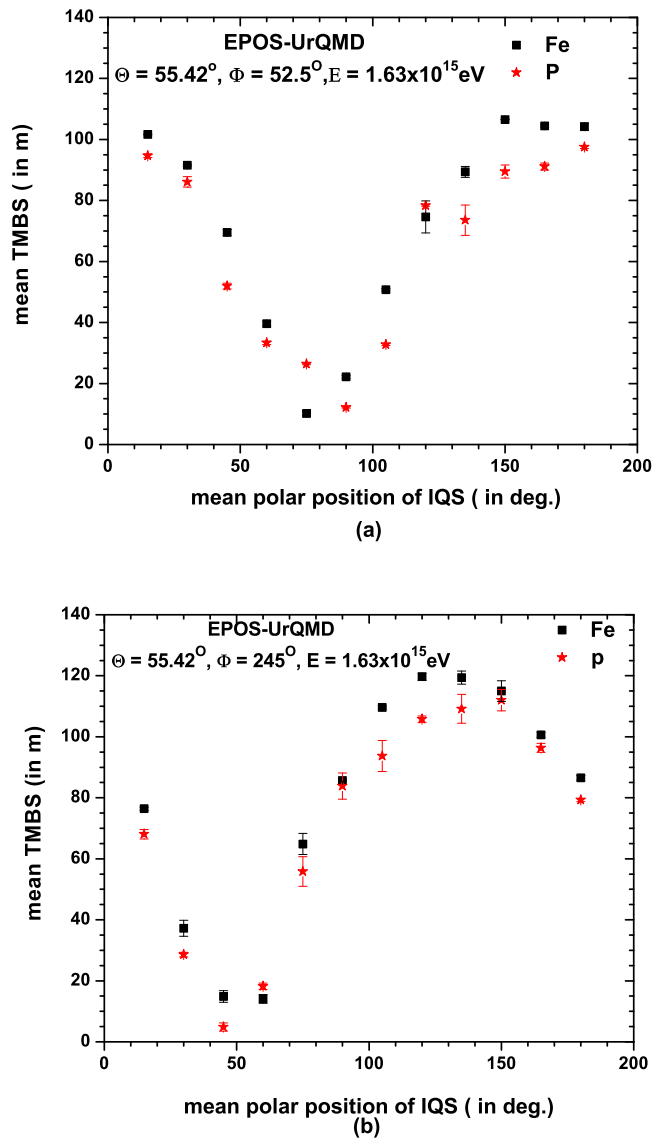
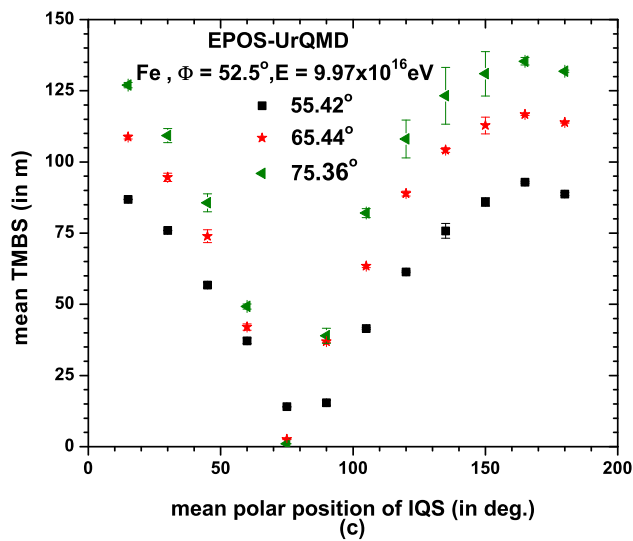
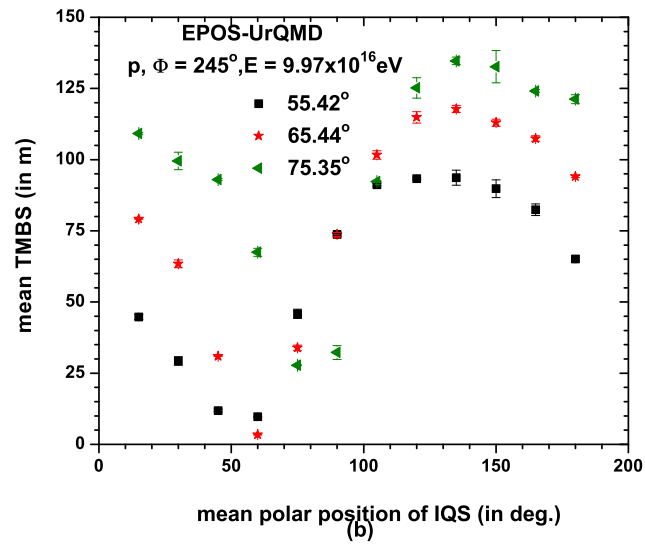
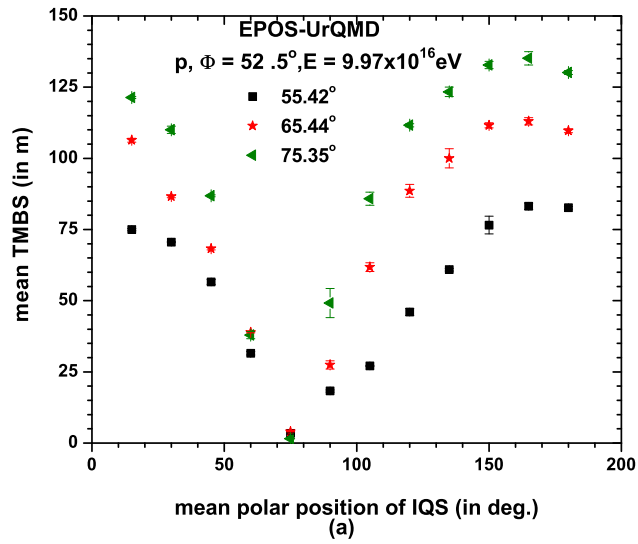


FIGURE 7.8: Polar variation of the mean TMBS for p and Fe showers arriving from two average arbitrary directions.

250° at $\langle\Theta\rangle = 55.42^\circ$ in the primary energy interval of 1 to 3 PeV. It is expected that μ^+ particles experience GF greatly around polar angles $\sim 165^\circ$ while μ^- around $\sim 345^\circ$ (peaks in the Fig 7.6a on shower plane) when $\langle\Phi\rangle \sim 52.5^\circ$. For $\langle\Phi\rangle \sim 245^\circ$, the Fig. 7.6b shows these peaks around polar angles $\sim 132^\circ$ and $\sim 312^\circ$ respectively. The TMBS accordingly takes higher values corresponding to the orientation of the IQS through $\sim 165^\circ - 345^\circ$ in the shower plane, which is reflected in the Fig. 7.8a for $\langle\Phi\rangle \sim 52.5^\circ$. On the other hand, the GF effects on the muon component for showers coming from the direction with $\langle\Phi\rangle \sim 245^\circ$, the nature of the variation of the TMBS is exhibited in the Fig. 7.8b. In this case



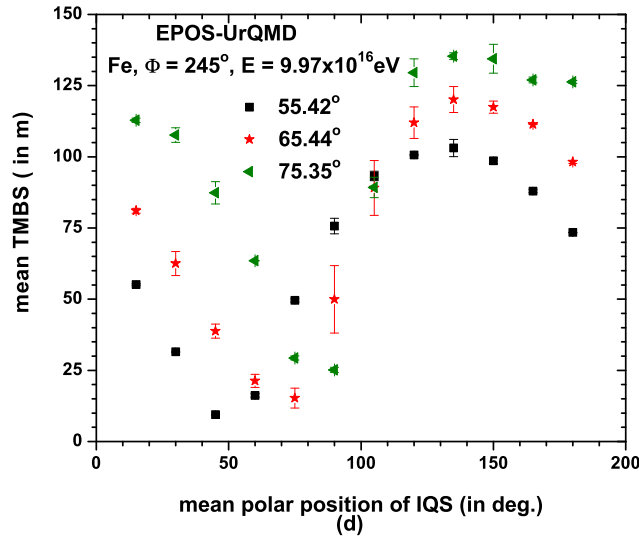


FIGURE 7.9: Comparison of the polar variations of TMBS for p and Fe showers arriving at different zenith angles of incidence for $\langle\Phi\rangle \sim 52.5^\circ$ and $\langle\Phi\rangle \sim 245^\circ$.

the maximum value of the TMBS parameter is found along the $\sim 132^\circ - 312^\circ$ orientation of the IQS. It is found that the TMBS is greater for Fe compared to p initiated showers in all the cases.

In Figs. 7.9a - 7.9d, we have repeated the same study independently for p and Fe primaries for $\langle\Phi\rangle = 52.5^\circ$ and 245° . Different curves in each of the Fig. 7.9 correspond different Θ of incidence of showers. As Θ increases more higher values for the parameter TMBS result in accordance with our expectation. The polar distribution of muons exhibits more and more asymmetry with increasing Θ and such a feature is reflected through the gradual increase of TMBS in the neighbourhood of polar angles $\sim 165^\circ$ and $\sim 132^\circ$ corresponding to $\langle\Phi\rangle \sim 52.5^\circ$ and $\sim 245^\circ$ respectively irrespective of primaries.

To assign a single TMBS to each shower, instead of its multiple values corresponding to various positions of the IQS over the polar angle range $0^\circ - 180^\circ$, we have introduced a mean maximum TMBS i.e. the MTMBS, which is the average of about four TMBS values for four different polar positions of the IQS over the polar angle between $\sim 150^\circ$ to $\sim 195^\circ$ (between $\sim 330^\circ$ to $\sim 375^\circ$ is the region for IQS in the opposite side) when $\Phi = 47.5^\circ - 57.5^\circ$. For $\langle\Phi\rangle = 245^\circ$, the MTMBS is estimated by taking average of TMBSs from the polar angle range between $\sim 120^\circ$ to $\sim 165^\circ$ (opposite side: between $\sim 300^\circ$ to $\sim 345^\circ$). The parameter

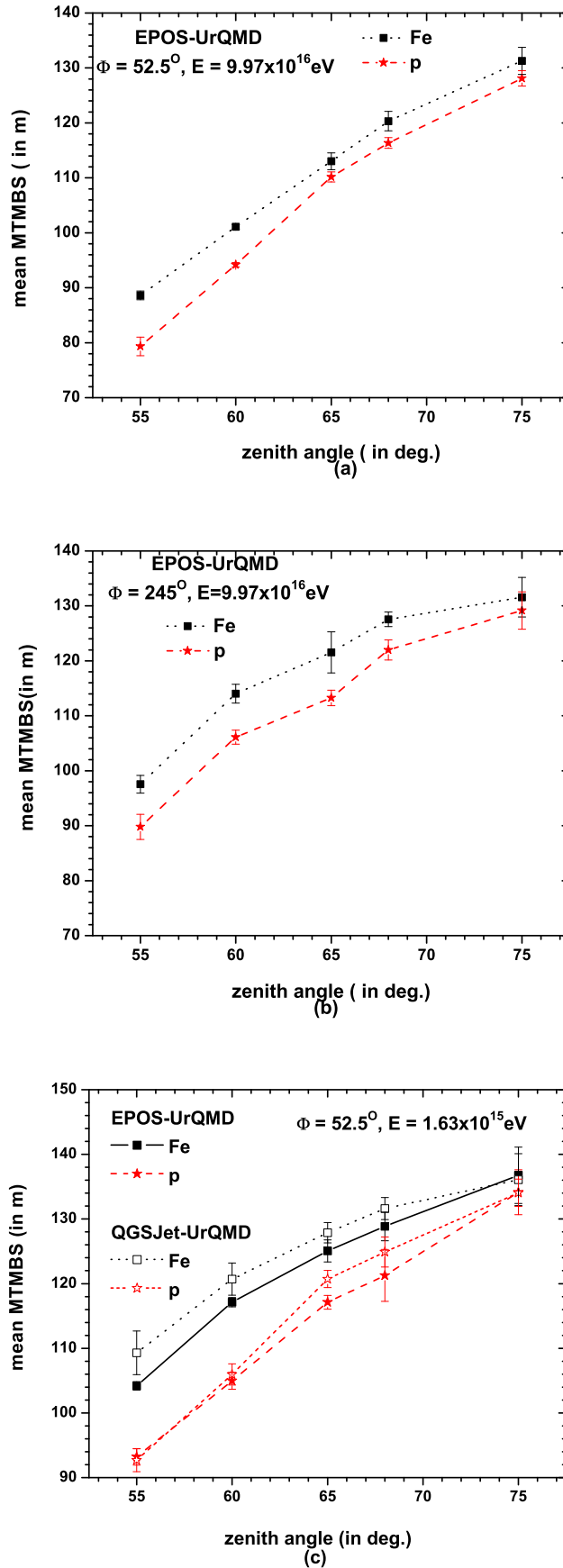


FIGURE 7.10: Variation of the mean MTMBS with Θ and dependence on the high-energy hadronic interaction models. Model dependence is shown through the figure (c). The lines are only a guide for the eye.

MTMBS shows sensitivity to the primary mass of CRs and hence the parameter can be used for the measurement of CR mass composition. An experimental approach for the estimation of the MTMBS parameter in a ground-based EAS experiment in association with muon detectors will be discussed in the section 7.6.

The variation of MTMBS against Θ is shown in Fig. 7.10a and Fig. 7.10b for showers induced by p and Fe, with $\langle\Phi\rangle \simeq 52.5^\circ$ and $\simeq 245^\circ$ respectively at $\langle E\rangle = 9.97 \times 10^{16}$ eV. The MTMBS values are higher for Fe compared to p primaries in all the cases irrespective of Θ , Φ , E and high-energy hadronic models. According to the Fig. 7.10a, the MTMBS values for p and Fe showers are approaching closer to one another as Θ increases. In Fig. 7.10c, we have presented the effect of high-energy hadronic models on the parameter under consideration. Results obtained from the EPOS look little better (consistent variation with Θ) in comparison with the QGSJet as far as the composition study of CRs is concerned. Errors for the MTMBS parameter are evaluated by averaging standard deviations in TMBS values within the polar angle range between 150° and 195° when $\langle\Phi\rangle = 52.5^\circ$ (i.e. $\langle\sigma\rangle = (\sum \sigma_i^2/4)^{\frac{1}{2}}, i = 1, \dots, 4$). For $\langle\Phi\rangle = 245^\circ$, averaging is done using values from the range $120^\circ - 165^\circ$.

7.5.3 Eccentricity parameter of the muon lateral distribution

The primary CR composition study has also been carried out using the eccentricity parameter (ϵ) of the polar asymmetric distribution of the muon component under the GF. We have defined the ϵ parameter as; $\epsilon = \sqrt{1 - (\frac{d_\perp}{d_\parallel})^2}$, where d_\parallel and d_\perp denote the core distances of a pair of points possessing the same muon density in an overall iso-density contour (elliptic) made by μ^+ and μ^- particles. One of the densities is estimated along an arbitrary axis which is being formed by the TMBS itself and the other, being \perp^r to the TMBS axis passing through the EAS core in the shower plane. Actually, μ^+ and μ^- in inclined showers under the GF are distributed asymmetrically in the shower plane (μ^+ and μ^- distributions also develop elliptic contours covering smaller regions but with an overlapping region). Combination of these smaller contours of μ^+ and μ^- will appear as an overall pattern which is equivalent to an iso-density ellipse. Such a pattern of the combined elliptic contour resulting from a pair of smaller iso-density contours

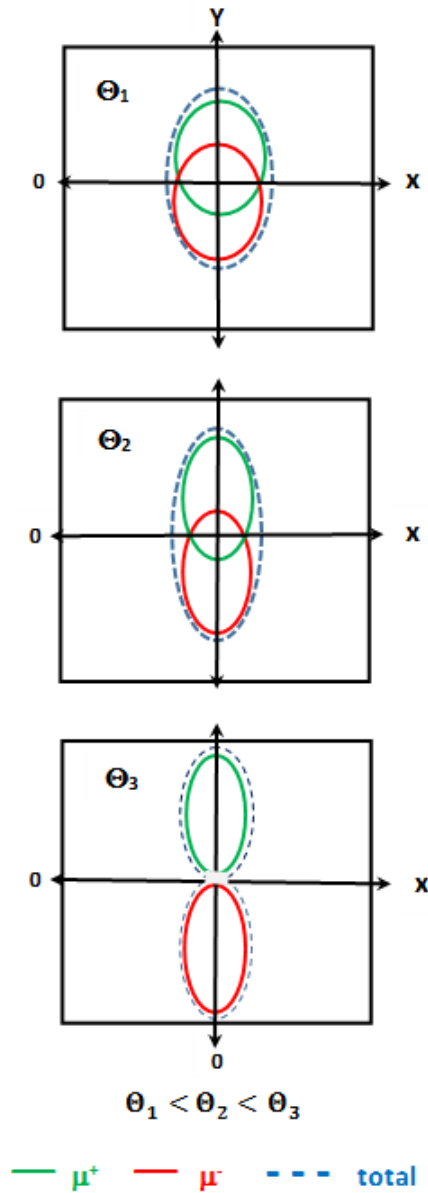


FIGURE 7.11: Combined elliptic contour resulting from a pair of smaller iso-density contours of μ^+ and μ^- with increasing Θ for $\Phi \sim 0^\circ$. At Θ_3 the overall ellipse gets 8-shaped pattern.

is presented by the sketch in the Fig. 7.11. The ϵ factors are evaluated by the above procedure at five $\langle\Theta\rangle$, ranging from 50° to 69° for p and Fe showers using the QGSJet and EPOS models. We have taken a very restrictive case with $\Phi = 0^\circ$ and $\langle E \rangle = 1.63$ PeV for this study and the results are shown in the Table 7.3. It reveals from the table that the lateral muon distribution in the shower plane gets more and more stretched along the axis constituted by the TMBS as Θ increases. Correspondingly the parameter ϵ increases as one moves from lighter to heavier primaries. It has been noticed that the parameter ϵ couldn't be estimated by the above procedure for showers with $\Theta \geq 75^\circ$. According to the Fig. 7.11, which is

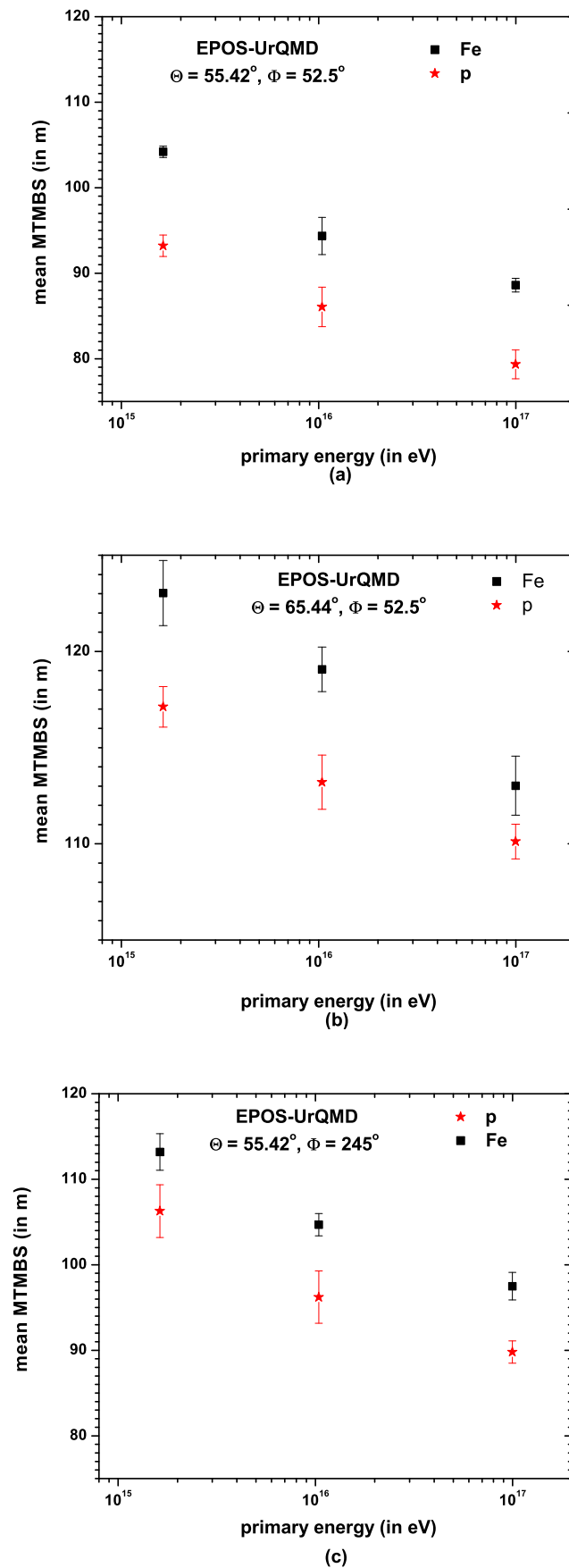
drawn at Θ_3 , the stretching of the muon lateral distribution along the TMBS axis is so high that iso-density concentric ellipse formation couldn't be possible (from iso-density ellipse to stretched out geometric 8-shaped density pattern develops). Hence the parameter cannot be useful for very inclined showers to measure the mass composition of CRs. The parameter ϵ gets higher values consistently for all Θ in the case of EPOS model compared to the QGSJet. In EPOS, there exists an additional particle production source which induces a larger number of muons from simulations with the model [36]. Hence, an increased number of muons come under the influence of the GF that would result into higher ϵ .

TABLE 7.3: The eccentricity parameters for showers initiated by proton and iron primaries and coming from the North direction: QGSJet model (Upper) and EPOS model (Lower).

Θ	50.23°	54.68°	59.72°	64.52°	68.3°
Proton	0.246 ± 0.011	0.422 ± 0.011	0.677 ± 0.014	0.706 ± 0.013	0.799 ± 0.012
Iron	0.406 ± 0.011	0.588 ± 0.014	0.702 ± 0.014	0.838 ± 0.012	0.910 ± 0.009
Proton	0.262 ± 0.005	0.406 ± 0.012	0.551 ± 0.013	0.721 ± 0.013	0.788 ± 0.012
Iron	0.427 ± 0.006	0.596 ± 0.014	0.708 ± 0.014	0.792 ± 0.014	0.913 ± 0.010

7.5.4 Variation of MTMBS with primary energy

From the experimental standpoint, the correlation of MTMBS with E or N_e has been considered as a basis for extracting information on the nature of primary CRs. The problem of determining the mass composition of CRs is a complicated one because many parameters in tandem are required. From the exploration of the geomagnetic spectroscopy it is found that parameters like TMBS, MTMBS and ϵ extracted from the asymmetric μ^+ and μ^- distributions are found sensitive to the CR mass composition. Practicability of the present approach to determine the CR mass composition requires a correlation between the observables MTMBS and E or N_e on an average shower with some $\langle\Theta\rangle$ corresponding to either $\langle\Phi\rangle = 52.5^\circ$ or 245° . It might be noted that the present approach on the measurement of primary mass composition with the observable TMBS or MTMBS; a new EAS technique, that is proposed first time using simulated showers, and therefore there is no scope to compare our predictions with available published data/results until now. In Fig. 7.12a and Fig. 7.12b, the variation for the mean MTMBS with $\langle E \rangle$ for p and Fe primaries are shown at $\langle\Theta\rangle = 55.42^\circ$ and 65.44° respectively for $\langle\Phi\rangle = 52.5^\circ$, corresponding to three primary energy regions used in this work.



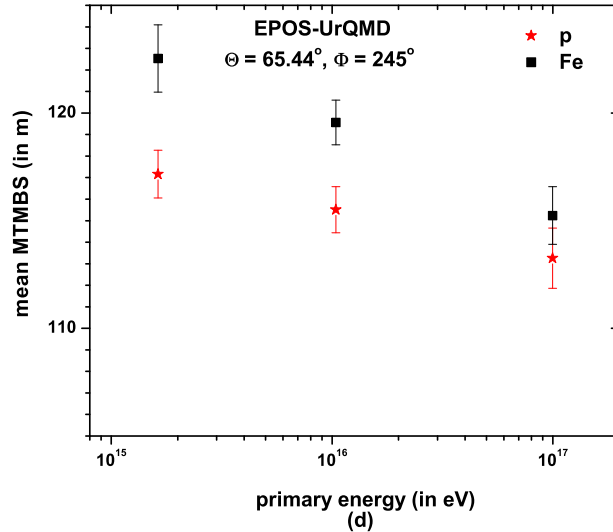


FIGURE 7.12: Variation of mean MTMBS with primary energy for p and Fe initiated showers coming the two arbitrarily selected directions: figure (a) and (b) correspond $\langle\Phi\rangle = 52.5^\circ$ while figure (c) and (d) for $\langle\Phi\rangle = 245^\circ$.

We repeat the same study for $\langle\Phi\rangle = 245^\circ$ and findings are shown in Fig. 7.12c and Fig. 7.12d.

7.5.5 EAS muons - Earth's magnetic field correlation

The MTMBS parameter obtained from μ^+ and μ^- asymmetries in an EAS solely due to the GF can now be exploited to estimate Earth's magnetic field in an unknown place having certain geographical latitude and longitude. We have used only proton and iron initiated showers with a fixed energy 10^{15} eV here. The steering file in the CORSIKA 6.970 code is made ready for two situations: (i) $\Theta = 50^\circ$ and $\phi = 0^\circ$, (ii) $\Theta = 60^\circ$ and $\phi = 55^\circ$. For a particular known location with geographical latitude and longitude the total magnetic field (B) and its horizontal (B_H), and vertical (B_V) components are required to be available from any scientific research organization like NOAA. By applying the present technique in terms of the MTMBS parameter, the field components B, B_H and B_V can be predicted of a location with known latitude and longitude.

Particularly for this study, we have chosen two different sets of geographical locations. Table 7.4 assembles few locations with fixed latitude (longitude is a

variable). Similarly, Table 7.5 presents few locations with fixed longitude (latitude is a variable). We have generated about 10^3 M C showers for each location corresponding to different magnetic field components obtained from NOAA.

TABLE 7.4: Details of the geomagnetic field components of some geographical locations with nearly constant latitude.

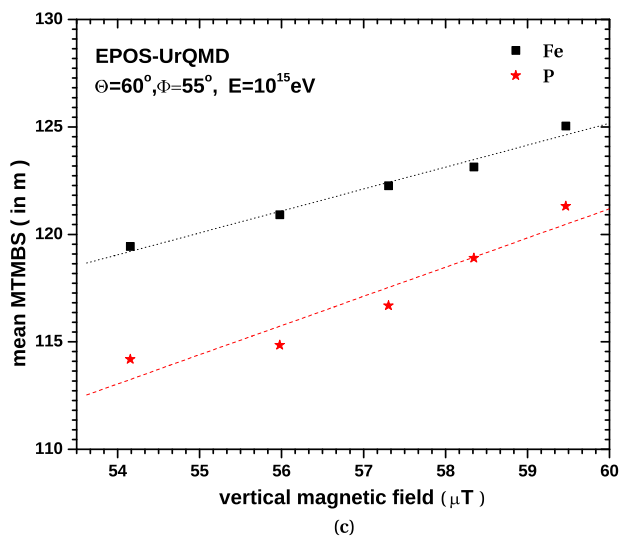
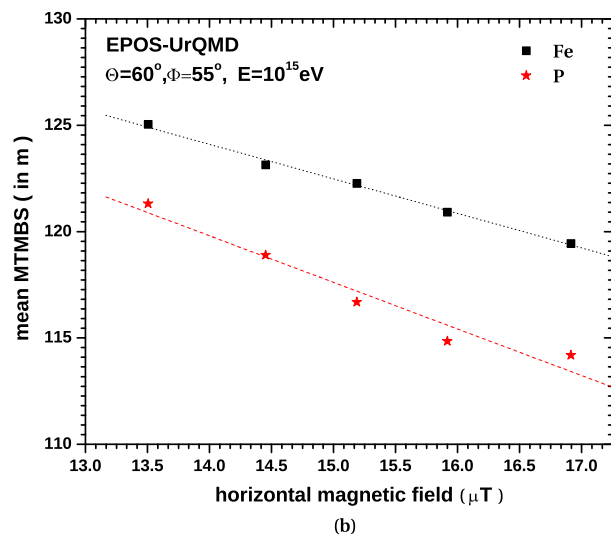
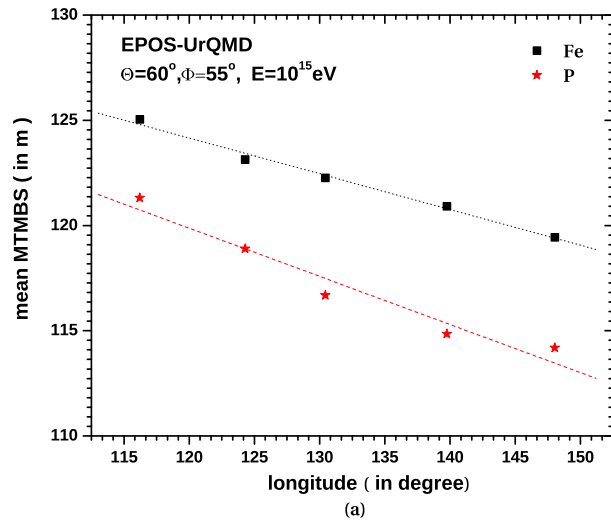
Geographical places	Latitude	Longitude	$B_H(\mu T)$	$B_V(\mu T)$	$B(\mu T)$
Talon	60.41385	148.02429	16.9138	54.1537	56.7336
Khabaresvsk rep.	60.75916	139.76257	15.917	55.977	58.0214
Sakha rep.	60.23981	130.44616	15.1874	57.3055	59.2839
Aldanskya Sakha rep.	60.15244	124.29382	14.4524	58.3457	60.109
Nyuya	60.06484	116.20789	13.506	59.4667	60.981

TABLE 7.5: Details of the geomagnetic field components of some geographical locations with nearly constant longitude.

Geographical places	Latitude	Longitude	$B_H(\mu T)$	$B_V(\mu T)$	$B(\mu T)$
Angola	-11.5230	16.907949	19.6794	-124.6477	31.5402
Rep. of Congo	-1.93323	16.715698	27.7198	-17.729	32.9045
Cameroon	7.1881	16.715698	33.4432	-5.8773	33.9557
Chad	15.79225	16.715698	35.2796	7.6818	36.1238
Libya	21.12549	16.715698	34.6308	16.0294	38.1606

As we know that the polar distributions of μ^+ and μ^- are affected due to GF and hence any variation in the GF components should change in the MTMBS parameter. It is known that Earth's magnetic field does not vary considerably with time but its intensity is not uniform across the globe with different latitude and/or longitude. In Fig. 7.13a, Fig. 7.13b, Fig. 7.13c and Fig. 7.13d, we have shown the variation of the MTMBS parameter with the longitude of five locations (Table 7.4) and different GF components. Similar kind of studies have also been carried out for the geographical locations according to the Table 7.5 with varying latitude, and these variations are displayed in Fig. 7.14a, Fig. 7.14b, Fig. 7.14c and Fig. 7.14d.

The dependence of the MTMBS parameter upon GF components of different geographical locations indicates that there should be a correlation between the MTMBS parameter arising out of the asymmetric μ^+ and μ^- distributions with various GF components. If an unknown geographical place is fallen across either at any location between the places with fixed longitude (Table 7.5) or fixed



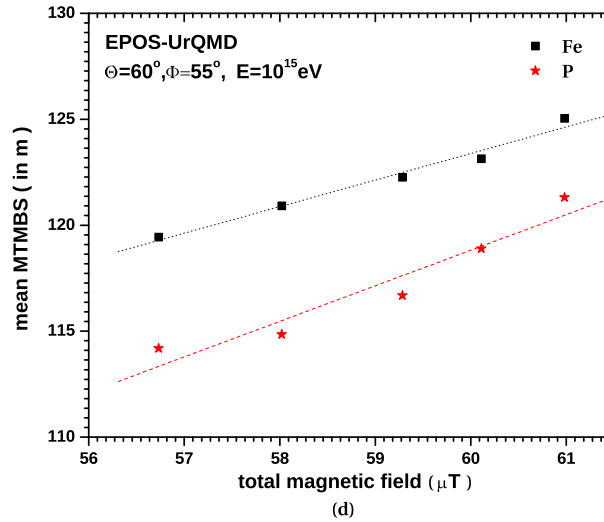


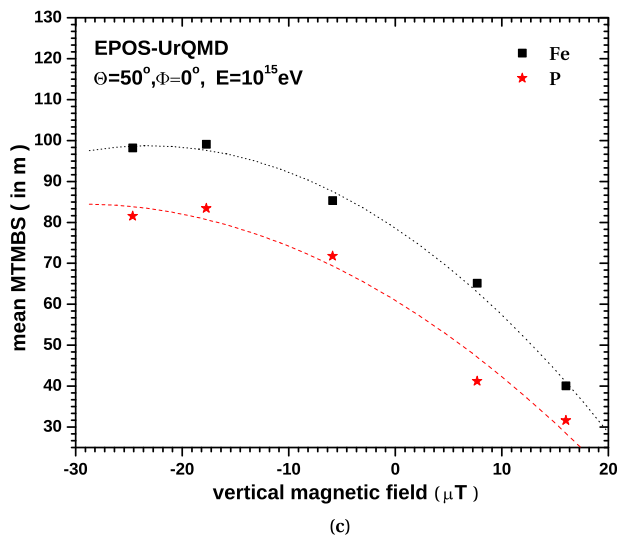
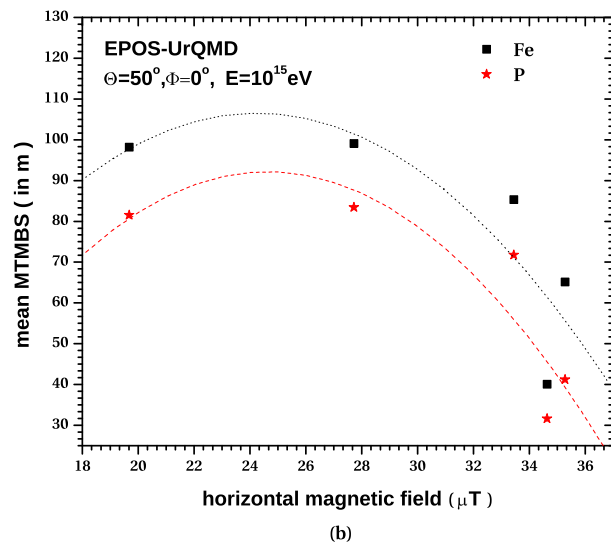
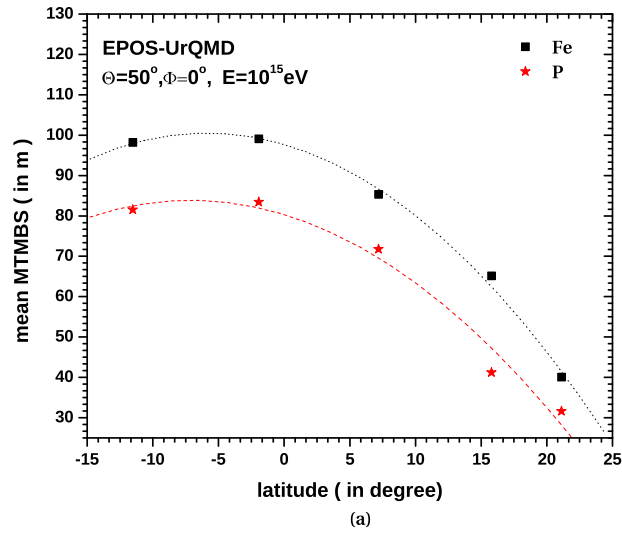
FIGURE 7.13: Variation of MTMBS parameter with longitude and different GF components.

latitude (Table 7.4), one should then estimate the GF components of the place by knowing the MTMBS parameter from μ^+ and μ^- distributions. Then the MTMBS parameter with the application of plots in Fig. 7.13 and Fig. 7.14 could predict the GF components. To check the reliability of the stated technique we have selected two geographical locations (places A and B) with known values of GF components from NOAA as a case study. By applying the present technique the MTMBS parameter are estimated using both the proton and iron showers and is displayed in Table 7.6. The corresponding GF components can be predicted by knowing the MTMBS parameter and then compare them with NOAA data. In Table 7.7 and Table 7.8 such comparative analyses are presented.

TABLE 7.6: Details of latitude, longitude and GF components for two geographical locations

Place	Azimuth angle	Zenith angle	Latitude	Longitude	$B_H(\mu T)$	$B_V(\mu T)$	$B(\mu T)$	MTMBS(m)	
								Iron	Proton
A	0°	55°	3.140516	16.694756	31.308	-11.6432	33.4035	89.185	74.031
B	55°	60°	60.63012	135.140076	15.4838	56.5948	58.6747	123.134	112.559

For the location A, we have used known latitude and estimated MTMBS as supplied parameters in order to extract the corresponding unknown quantities such as longitude and GF components from the plots in Fig. 7.13. We take known longitude and estimated MTMBS, both as supplied parameters for the location B



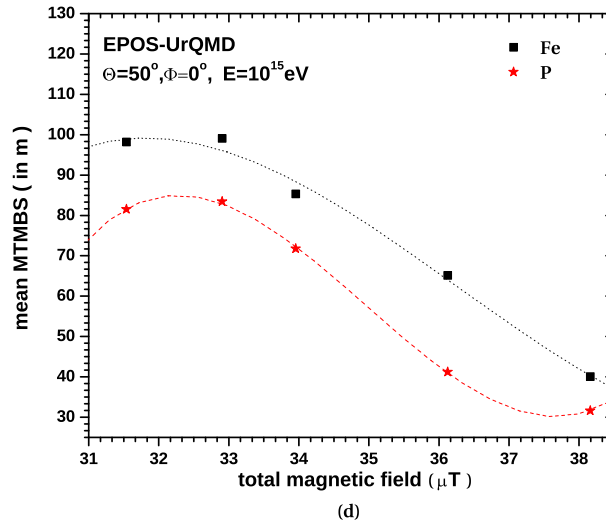


FIGURE 7.14: Variation of MTMBS parameter with latitude and different GF components.

to extract unknowns like latitude and GF components from the plots in Fig. 7.14. Our results extracted from the plots are given in Table 7.7 and Table 7.8.

TABLE 7.7: Latitude and GF components for the geographical location A, obtained from Fig. 7.14

Parameters	Iron	Proton	Data from NOAA [†]
Latitude	6.129704	4.81498	3.140516
$B_H(\mu T)$	31.5321	30.8672	31.308
$B_V(\mu T)$	-7.1886	-7.1886	-11.6432
$B(\mu T)$	33.8353	33.8120	33.4035

[†]National Oceanic and Atmospheric Administration (<https://www.noaa.gov/>)

TABLE 7.8: Longitude and GF components for the geographical location B, obtained from Fig. 7.13

Parameters	Iron	Proton	Data from NOAA
Latitude	126.0148	153.1951	135.140076
$B_H(\mu T)$	14.59649	17.35841	15.4838
$B_V(\mu T)$	59.3586	53.7028	56.5948
$B(\mu T)$	58.00275	58.9539	58.6747

7.5.6 Solar activity and Earth's magnetic field

The Earth's magnetic field due to some of its internal mechanisms varies very slowly with time, but during solar activity a sudden change is observed in its GF.

This sudden change in GF must affect the distribution of energetic muons in an EAS and hence the MTMBS parameter. The solar activity directs oppositely to the GF and hence the GF intensity weakens.

To investigate the effect of a sudden weakening in GF during solar activity on EAS muons (actually on MTMBS), we have reduced the vertical component of earth's magnetic field (B_V) in the CORSIKA steering file in three cases; (i) $0.70\mu T$, (ii) $1.00\mu T$ and (iii) $2.00\mu T$, keeping the horizontal component unchanged. We have simulated only iron showers at the KASCADE level (110 m a.s.l.) here, with $E = 98 - 102$ PeV. Near the KASCADE site we have also performed simulation by adopting the above procedure at different (or higher) altitude (1608 m a.s.l.). Our results from these studies are displayed in Table 7.9 and 7.10 respectively. No considerable variation in the MTMBS parameter is noticed due to any transient weakening of the GF caused by the solar activity. However at higher altitude the activity is slightly more.

TABLE 7.9: Simulation results at KASCADE level with reduced magnetic field.

Primary particle	Zenith angle	Azimuth angle	$B_H(\mu T)$	$B_V(\mu T)$	Change in $B_V(\mu T)$	MTMBS (m)	Error (m).
Fe	65°	52.5°	20.52	43.57	0.00	113.023	1.537
Fe	65°	52.5°	20.52	42.87	0.70	113.684	0.577
Fe	65°	52.5°	20.52	42.57	1.00	112.915	0.532
Fe	65°	52.5°	20.52	41.57	2.00	112.259	0.616

TABLE 7.10: Simulation results at a nearby level of KASCADE experiment with reduced magnetic field.

Primary particle	Zenith angle	Azimuth angle	$B_H(\mu T)$	$B_V(\mu T)$	Change in $B_V(\mu T)$	MTMBS (m)	Error (m).
Fe	65°	52.5°	22.22	41.99	0.00	109.743	0.573
Fe	65°	52.5°	22.22	41.29	0.70	107.944	0.558
Fe	65°	52.5°	22.22	40.99	1.00	107.552	0.559
Fe	65°	52.5°	22.22	39.99	2.00	107.360	0.608

7.6 Experimental approaches and concluding remarks

It has been found from our analysis that the influence of Earth's magnetic field plays an important role for detailed features of muons lateral distribution at least for highly inclined showers. The proposed method takes into account the polar

asymmetry of muon distribution to determine the primary CR mass composition at KASCADE level. This analysis uses proton and iron initiated simulated showers corresponding to three narrow primary energy regions, and two selected azimuthal angle ranges centered around 52.5° and 245° respectively. There is a scope to extend the present analysis to a much wider primary energy range in order to get an indication of any possible change in the mass composition of PCR with energy. This approach can be carried out for other geomagnetic positions as well to correlate important geomagnetic properties with high-energy astro-particle phenomena.

Our analysis concerning the effects of the GF on the muon component of inclined EASs reveals several interesting features such as polar asymmetries of μ^+ and μ^- , sectoral muon abundances, elliptic footprints of their lateral distributions, and amplitude of fluctuations between proton and iron induced showers. Taking a small sample of data such effects are also found to persist with comparable magnitude (not shown here) if we replace the UrQMD code in the simulation by the Fluka [37] in the treatment of low energy hadron collisions.

The present method might help to design EAS arrays in association with muon detectors to derive more information about the primary CRs employing the trio **the EAS direction** (Θ and Φ), **the EAS core** (x_o, y_o) and **the geomagnetic field**. The measurement of the sign of the muon charge in an EAS is of considerable interest for different aspects of astroparticle physics. Most of the experimental techniques relating the muon charge sign determination used magnetic spectrometers with different limitations. The measurement of the muon charge sign is the first point in the concept of designing of any experiment by exploiting the present method. In addition, this analysis also requires the information of the point of impact of each muon in the location of a muon detecting system. Therefore, any magnetized detecting system cannot be a good ploy to extract the information of the location of a muon resulting from the geomagnetic effect only.

In the context of this work, a muon detecting system consisting of shielded scintillators is expected to be capable to measure the muon charge sign by estimating the life time of the muons stopped in a stack unit of vertically arranged active (plastic scintillator sheets) and passive (aluminum plates) layers. The proposed layout foresees two muon detecting systems containing several such stack units covering the two selected regions in diametrically opposed position. The height

of the stack unit of alternatively arranged active and passive layers, and the required size of the e/γ shielding (concrete and lead layers) at the top of the detecting systems to observe muons with $E_{\mu}^{\text{Th.}} \geq 100$ GeV can be fixed by the detector simulations. Each of the unit is exactly similar to a single WILLI detector used in early works [19].

Aluminum absorber is used to separate positive and negative muons in the experimental setup. The mean lifetime of negative muons is quite smaller than the mean lifetime of positive muons. The method of delayed coincidences is used to distinguish positive and negative muons which are brought to rest in the system. The negative muon is captured by the host atom (aluminum, and carbon in plastic) forming a muonic atom that subsequently undergoes decay and further capture within a short time. While the positive muons follow only free decay and effectively survive longer duration compared to negative muons. Hence, a significant difference in the mean lifetime of negative muons in aluminum compared to that of the free decay of positive muons is registered by some simple time electronics with reasonably high rates.

The discrete stack units of each muon detecting system provide the detection point of a muon. The midpoint coordinate of a line connecting the two diagonally placed photomultiplier tubes in an active element is used as the position of detection of a muon. The two muon detecting systems are rotatable to be directed in a particular direction to measure the incoming muons corresponding to different Θ and Φ . The mid point coordinates of all the diagonals connecting a pair of photomultiplier tubes in an active element are provided from the Monte Carlo simulations for different combinations of $\Theta \geq 55^{\circ}$ and $\Phi \sim 52.5^{\circ}$ or $\sim 245^{\circ}$ in particular. With the help of the simulations a weight average of all the positive and negative muons from both the muon detecting systems in an experiment can be estimated separately.

As mentioned above, the EAS experimental setup should have a close-packed detector array (200 m x 200 m for KASCADE) for determining global parameters of an EAS (Θ , Φ , N_e and x_o, y_o etc.). It should be mentioned that for a closely packed array, estimation for the EAS core location by simple weight averaging of particle (e^{\pm}) densities from discrete detector locations does not differ appreciably from the core obtained from the shower reconstruction. The estimation of the main parameter i.e. the MTMBS needs suitable positioning of the pair of muon

detectors covering two diagonally opposed regions; $159^\circ - 169^\circ$ and $339^\circ - 349^\circ$ in a possible experimental layout shown in the Fig. 7.15 for $\langle \Phi \rangle \simeq 52.5^\circ$. Two uncovered sectors in the Fig. 7.15 between the pair of dotted lines for each, in opposed positions within the polar regions of $127^\circ - 137^\circ$ and $307^\circ - 317^\circ$ are shown for showers with $\langle \Phi \rangle \simeq 245^\circ$. The proposed muon detector couple provides a limited muon detection area of $\sim 785 \text{ m}^2$ from the point of view of their production cost. However, the best option would be a complete annular region covering muon detector (region between the radii 60 m and 90 m from shower core), and for each shower event according to the Φ value. Such an arrangement requires a very large muon detector with an area $\sim 14137 \text{ m}^2$ for the present purpose, and that lacks practical feasibility. With the present muon detector layout, it is found that the event selection has to be limited to two narrow Φ windows. The required resolution of the EAS array should be consistent with the physics

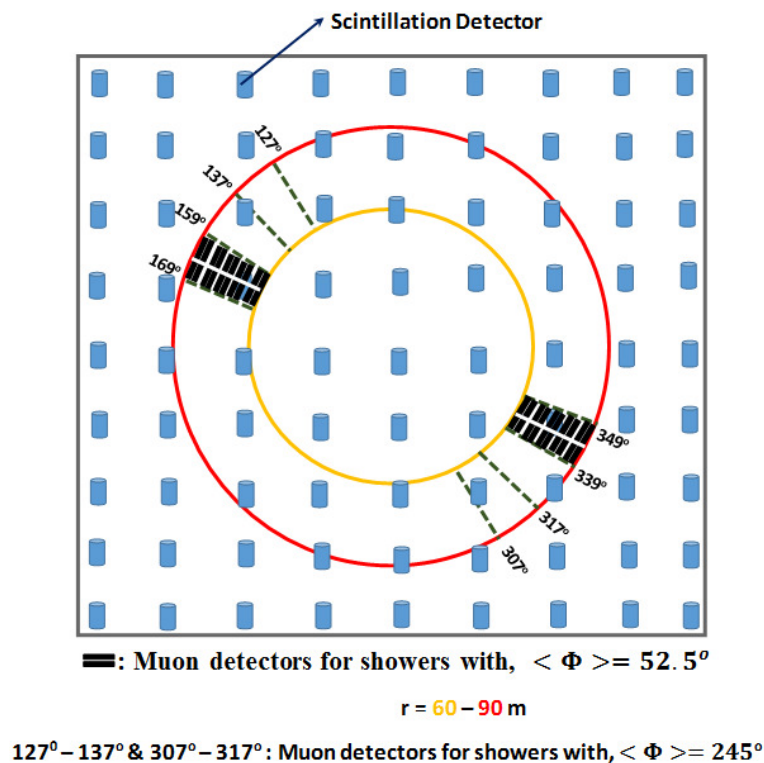


FIGURE 7.15: Sketch of a possible array layout containing number of scintillation detectors and two muon detecting systems for practical realization of the proposed EAS method.

requirements of the proposed method in an experiment. As already explained in the text that the method requires highly inclined showers ($\Theta \geq 55^\circ$). Moreover, the geomagnetic conditions at KASCADE level drive a relatively higher percentage of showers through two azimuthal directions according to the Fig. 7.5. In an

EAS experiment, a rough idea of the angular resolution of the array can be obtained if the time resolution (Δt) that results from the width of a shower disk and instrumental timing error from two identical array detectors is known. The conventional ‘split’ array method is being used for estimating the angular resolution of the array at sea level in both the angular coordinates Θ and Φ [38].

The present method is applied to showers which are generated almost at three fixed primary energies. On the other hand, if the array takes densely packed shower detectors, the error of the core position is expected to be very marginal and hence the x, y coordinates of muons with respect to the core position can be estimated accurately. Therefore, we have made efforts to investigate the angular resolution of the array (i.e. lower limits on angular coordinates Θ and Φ) from the analysis of the MTMBS parameter. To get an idea about the required Θ resolution we have generated 20 showers each for p, He and Fe primaries at fixed $\Phi = 52.5^\circ$, $E = 100$ PeV and $\Theta = 55^\circ$. We repeat the same at those fixed $\Phi = 52.5^\circ$ and $E = 100$ but at different $\Theta = 56^\circ, 57^\circ, \dots, 65^\circ$. For each case, we have estimated the corresponding MTMBS parameter. We have observed that if two p showers maintain a minimum of $\geq 2^\circ$ Θ difference ($\delta\Theta$) then the MTMBS parameter could discriminate them including errors even at fixed Φ and E . For He and Fe, we have got the same resolution for Θ at these conditions. Under the same conditions, the MTMBS parameter may discriminate between p and He showers with $\delta\Theta \simeq 1^\circ$. We have applied the same procedure for the estimation of the required Φ resolution. Here Θ and E are fixed at values 55° and 100 PeV but Φ varies as $5^\circ, 10^\circ, \dots, 135^\circ$ in each case. The resolution in Φ for the same type of primaries i.e. either p or He or Fe is closer to an average value $\simeq 7.5^\circ$ while for p and He it comes out as $\simeq 2^\circ$. A summary of the angular resolution study of our proposed array with the help of MTMBS parameter is provided in the Table 7.11 and Table 7.12. Although we have not verified yet but it is expected that the array resolution in terms of Θ may deteriorate beyond 65° .

In the Fig. 7.15, each smaller black top surface refers a lead shielding above a WILLI type muon detector unit which is set at the threshold energy 10^2 GeV for muons. It would be an interesting task to apply such a method using observed EAS data if the KASCADE or GRAPES - 3 experiments runs with the facility of concurrent muon measurements [39] introducing WILLI type muon detecting

TABLE 7.11: Analysis showing azimuthal dependence of MTMBS parameter for $\theta = 55^\circ$ and $E = 100$ PeV. Column 2 and 3 for proton initiated showers while column 4 and 5 for iron initiated showers.

Azimuthal angle	MTMBS (m)	Error	MTMBS (m)	Error
5°	66.16	± 0.33	69.33	± 1.63
15°	64.91	± 1.14	73.43	± 0.61
25°	66.08	± 0.92	75.85	± 2.07
35°	73.68	± 1.49	82.34	± 1.04
45°	75.74	± 1.56	86.52	± 1.16
55°	82.74	± 0.42	91.55	± 0.94
65°	86.31	± 0.47	94.54	± 1.14
75°	90.40	± 1.52	96.34	± 3.34
85°	92.81	± 1.17	101.53	± 0.39
95°	94.53	± 1.07	103.04	± 1.26
105°	100.67	± 0.71	103.10	± 0.81
115°	100.67	± 0.71	107.25	± 1.27
125°	100.68	± 1.02	105.01	± 1.33
135°	101.54	± 1.56	108.17	± 1.44

TABLE 7.12: Analysis showing zenith angle dependence of MTMBS parameter for $\Phi = 52.5^\circ$ and $E = 100$ PeV. Column 2 and 3 for proton initiated showers while column 4 and 5 for iron initiated showers.

Zenith angle	MTMBS (m)	Error	MTMBS (m)	Error
56°	84.15	± 0.52	91.43	± 2.08
57°	87.18	± 2.41	93.18	± 0.39
58°	88.70	± 1.38	96.78	± 1.89
59°	90.81	± 1.06	101.50	± 0.53
60°	94.17	± 0.39	101.09	± 0.39
61°	98.34	± 1.81	103.43	± 0.67
62°	100.50	± 2.21	106.18	± 0.81
63°	104.73	± 1.43	107.78	± 1.04
64°	106.68	± 0.94	112.50	± 2.02
65°	110.17	± 0.90	113.02	± 1.54

units instead of their existing systems. A new experiment consisting of underground installations of muon detectors and an EAS array on the ground plane is expected to be more appropriate for the study. The main sources of error are the fluctuations in muon numbers from shower to shower, non-uniform behavior of the local geomagnetic field, and the uncertainties in arc, and radial distance estimations using x,y coordinate values of each muon within a polar region of the selected IQS.

The present analysis is also found capable to measure the unknown GF components of a location. A correlation between any transient weakening of the GF due

to solar activity and the corresponding asymmetries in μ^+ and μ^- distributions of a CR induced EAS has been noticed.

Bibliography

- [1] Greisen, K.: *Progress in Cosmic Ray Physics III*. North Holland, Amsterdam, **3** 1 (1956)
- [2] Apel, W.D. *et al.*, *Astropart. Phys.*, **24** 467–483 (2006)
- [3] Heck, D. *et al.*: The CORSIKA Air Shower Simulation Program Forschungszentrum Karlsruhe Report FZK6019 (1998)
- [4] Cocconi, G. *Phys. Rev.*, **93** 646 (1954)
- [5] Abraham, J. *et al.*, *Phys. Rev. Lett.*, **104** 091101 (2010)
- [6] Allan, H.R. *et al.*, *Nature* **222** 635–637 (1969)
- [7] Allkofer, O.C. *et al.*, *J. Geophys. Res.*, **90** 3537 (1985)
- [8] Bowden, C.C.G. *et al.*, *J. Phys. G: Nucl. Part. Phys.*, **18** L55 (1992)
- [9] Browning, R., Turver, K.E. *Nuovo Cimento A* **38** 223 (1977)
- [10] Capdevielle, J.N., Gall, Le, C., Sanosyan, K.h.N. *Astropart. Phys.*, **13** 259 (2000)
- [11] Chadwick, P.M. *et al.*, *J. Phys. G: Nucl. Part. Phys.* **25** 1223 (1999)
- [12] Cillis, A., Sciutto, S.J. *J. Phys. G: Nucl. Part. Phys.* **26** 309 (2000)
- [13] Colgate, S.A. *J. Geophys. Res.* **72** 4869 (1967)
- [14] Ivanov, A.A. *et al.*, *JETP Letts.* **69** 288 (1999)
- [15] Lang, M.J. *et al.*, *J. Phys. G: Nucl. Part. Phys.* **20** 1841 (1994)
- [16] Ave, M., Vasquez, R.A., Zas, E. *Astropart. Phys.*, **14** 91 (2000)
- [17] Muniz, J.A. *et al.*, *Astropart. Phys.*, **59** 29 (2014)

- [18] Porter, N.A. *Lettere Al Nuovo Cimento Series 2* **8** 481 (1973)
- [19] Rebel, H. *et al.*, *J. Phys. G: Nucl. Part. Phys.* **35** 085203 (2008)
- [20] Sima, O. *et al.*, *Nucl. Instru. Meth. A* **638** 147 (2011)
- [21] The Pierre Auger collaboration: The effect of the geomagnetic field on cosmic ray energy estimates and large scale anisotropy searches on data from the Pierre Auger Observatory. *JCAP* **11** 022 (2011)
- [22] Engel, R., Heck, D., Pierog, T. *Annual Rev. Nucl. Part. Sc.* **61** 467–489 (2011)
- [23] Capdevielle, J.N., Dey, R.K., Bhadra, A. *33rd Int. Cosmic Ray Conf.* ISBN-978-85-89064-29-3 (2013)
- [24] Dam, S., Dey, R.K., Bhadra, A. In: Mandal, J.K. *et al.*, (eds.) *Proc. Information Systems Design and Intelligent Applications*, vol. **339** p. 1 (2015)
- [25] Kalmykov, N.N., Ostapchenko, S.S., Pavlov, A.I. *Nucl. Phys. B* **52** 17 (1997)
- [26] Werner, K., *et al.*, *Phys. Rev. C* **74** 044902 (2006)
- [27] Bleicher, M., *et al.*, *J. Phys. G: Nucl. Part. Phys.* **25** 1859 (1999)
- [28] Nelson, W.R., *et al.*: The EGS4 Code System Report SLAC265. Stanford Linear Accelerator Center, Stanford (1985)
- [29] National Aeronautics and Space Administration (NASA): US standard atmosphere Technical Report NASA-TM-X-74335 (1976)
- [30] Kobal, M. *Astropart. Phys.*, **15** 259 (2001)
- [31] Montanus, J.M.C. *Exper. Astron.*, **41(1)** 159–184 (2016)
- [32] Antoni, T., *et al.*, *Astropart. Phys.* **19** 703–714 (2003)
- [33] Arteaga, J.C., *et al.*, *Proc. of 30th ICRC Mexico* **4** 203–206 (2008)
- [34] Arteaga-Velázquez, J.C., *et al.*, *Nucl. Phys. B (Proc. Suppl.)* **196** 183–186 (2009)
- [35] Dey, R.K., Dam, S., Ray, S. *Indian J Phys.* (2016). doi:10.1007/s12648-016-0920-z

- [36] Pierog, T., Werner, K. *Phys. Rev. Lett.* **101** 171101 (2008)
- [37] Fassó, A., *et al.*, In: *Proc. Monte Carlo 2000 Conf.* (Lisbon), p. 955. Springer, Berlin (2001) Author's personal copy98 *Exp Astron* **43** 75–98 (2017)
- [38] Bhadra, A., *et al.*, *Nucl. Instr. Meth. Phys. Res. A* **414** 233 (1998).
- [39] Apel, W.D., *et al.*, *Astropart.Phys.* **65** 55–63 (2015)